Astronomy & Astrophysics

HH 223: a parsec-scale H$_2$ outflow in the star-forming region L723[*],[**]

R. López[1], J. A. Acosta-Pulido[2,3], G. Gómez[2,4], R. Estalella[1], and C. Carrasco-González[5]

[1] Departament d'Astronomia i Meteorologia (IEEC-UB), Institut de Ciències del Cosmos, Universitat de Barcelona, Martí i Franquès 1, 08028 Barcelona, Spain
e-mail: [rosario;robert.estalella]@am.ub.es
[2] Instituto de Astrofísica de Canarias, 38200 La Laguna, Tenerife, Spain
e-mail: jap@iac.es
[3] Departamento de Astrofísica, Universidad de La Laguna, 38205 La Laguna, Tenerife, Spain
[4] GTC Office, Spain
e-mail: gabriel.gomez@gtc.iac.es
[5] Instituto Astrofísica Andalucía, CSIC, Camino Bajo de Huétor 50, 18008 Granada, Spain
e-mail: gcharly@iaa.es

Received 1 June 2010 / Accepted 2 August 2010

ABSTRACT

Context. The dark cloud Lynds 723 (L723) is a low-mass star-forming region where one of the few known cases of a quadrupolar CO outflow has been reported. Two recent works have found that the radio continuum source VLA 2, towards the centre of the CO outflow, is actually a multiple system of young stellar objects (YSOs). Several line-emission nebulae that lie projected on the east-west CO outflow were detected in narrow-band Hα and [S II] images. The spectra of the knots are characteristic of shock-excited gas (Herbig-Haro spectra), with supersonic blueshifted velocities, which suggests an optical outflow also powered by the VLA 2 YSO system of L723.

Aims. Our aim is to study L723 in the near-infrared and look for line-emission nebulae associated with the optical and CO outflows.

Methods. We imaged a field of $\sim$5' $\times$ 5' centred on HH 223, which includes the whole region of the quadrupolar CO outflow with narrow-band filters centred on the [Fe II] 1.644 μm and H$_2$ 2.122 μm lines, together with off-line H_c and K_c filters. The [Fe II] and H$_2$ line-emission structures were identified after extracting the continuum contribution, if any. Their positions were determined from an accurate astrometry of the images.

Results. The H$_2$ line-emission structures appear distributed over a region of 5.'5 ($\sim$0.5 pc for a distance of 300 pc) at both sides of the VLA 2 YSO system, with an S-shape morphology, and are projected onto the east-west CO outflow. Most of them were resolved in smaller knotty substructures. The [Fe II] emission only appears associated with HH 223. An additional nebular emission from the continuum in H_c and K_c appears associated with HH 223-K1, the structure closest to the VLA 2 YSO system, and could be tracing the cavity walls.

Conclusions. We propose that the H$_2$ structures form part of a large-scale near-infrared outflow, which is also associated with the VLA 2 YSO system. The current data do not allow us to discern which of the YSOs of VLA 2 is powering this large scale optical/near-infrared outflow.

Key words. stars: formation – Herbig-Haro objects – infrared: ISM – ISM: jets and outflows

1. Introduction

Lynds 723 (L723) is an isolate dark cloud located at a distance of 300 ± 150 pc (Goldsmith et al. 1984) that shows evidence of low-mass star formation, and is the site where one of the few known cases of a quadrupolar CO outflow (two separate pairs of red-blue lobes; Lee et al. 2002, and references therein) has been reported. The 3.6 cm radio continuum source VLA 2 (Anglada et al. 1996), towards the centre of the CO outflow, harbours the source that powers the outflow. VLA 2 is embedded in high-density gas traced by NH$_3$, which shows evidence of gas heating and line broadening (Girart et al. 1997). Two recent works by Carrasco-González et al. (2008) and Girart et al. (2009)

report that VLA 2 is a multiple system. Carrasco-González et al. (2008) detect a system of four (VLA 2A, 2B, 2C and 2D) young stellar objects (YSOs) and propose that the morphology of the CO outflow is actually the result of the superposition of three independent pairs of CO lobes. They also propose that one of the YSOs (VLA 2A) is powering the largest, east-west pair of CO lobes and the system of emission-line optical nebulae, which is reminiscent of Herbig-Haro (HH) objects, first reported by Vrba et al. (1986). Girart et al. (2009) detect at 1.35 mm emission from dust, resolved into two components, SMA1 and SMA2, which have very similar physical properties. SMA2 seems to be in a more evolved stage and is harbouring a multiple low-mass protostellar system (VLA 2A, 2B and 2C). They also report emission from the SiO 5–4 line towards the SMA sources, this emission shows an elongated morphology that follows the northwest-southeast direction pointed by the larger CO outflow lobes, which traces a region of interaction between the dense envelope and the outflow.

In the optical wavelength range, deep Hα and [S II] narrow-band images of the L723 field were obtained by López et al. (2006). From these images, the knotty structure of the HH 223 "linear emission feature" (hereafter, we will refer to it as HH 223) detected by Vrba et al. (1986) was resolved into several knots, HH 223-A to -F, and the line-emission nature of other nebulae in the field was established. Long-slit spectroscopy covering the spectral range 5800–8300 Å was made by López et al. (2009) through HH 223. The spectra obtained are characteristic of shock-excited gas (HH spectra), both for the knots and for the low-brightness nebula surrounding the knots. The radial velocities derived for the knots are supersonic (blueshifted velocities, ranging from −60 to −130 km s^{-1}). The velocities derived for the low-brightness nebula are compatible with the ambient gas velocity.

In the near-infrared range, Palacios & Eiroa (1999) imaged a field of ~2′ centred on VLA 2 in the K band and detected H$_2$ emission from several nebulae located at both sides of VLA 2. However, the field imaged only partially covers L723: it does not include the complete region encompassed by the CO outflow and, in particular, only the western side of HH 223 was mapped. Furthermore, since the continuum was not subtracted from their narrow-band H$_2$ image, it is impossible to know whether there is continuum contribution to the emission in the nebula close to VLA 2. Continuum emission around this position is expected if the nebula is tracing a cavity opened by the molecular outflow.

We imaged the L723 field with narrow-band filters centred on the [Fe II] λ 1.644 μm and H$_2$ υ = 1–0 S(1) (λ 2.122 μm) lines together with the broad-band H and the off-line narrow-band H_c and K_c filters. Our aims were to get a more complete picture of the HH 223 outflow in the near-infrared wavelength range, to search for counterparts of the optical nebulae, and to establish the nature of the near-infrared emission coming from the nebulae of the L723 field. The main results are presented in this paper.

2. Observations, data reduction and calibration

Narrow-band images were obtained through filters centred on the [Fe II] and H$_2$ υ = 1–0 S(1) lines which is adequate to detect the emission from shocked ionized and molecular gas respectively. Additional images were obtained through the broad-band H filter and the narrow-band emission-line free filters H_c and K_c, which are useful to subtract the continuum from emission-line filters. Observations were made on 2006 July with the instrument LIRIS (Long-Slit Intermediate Resolution Infrared Spectrograph; Acosta Pulido et al. 2003) at the 4.2 m Williams Herschel Telescope (WHT) of the Observatorio del Roque de los Muchachos (ORM, La Palma, Spain). Details about the observations are listed in Table 1. LIRIS is equipped with a Rockwell Hawaii 1024 × 1024 HgCdTe array detector. The spatial scale is 0″25 pixel^{-1}, giving an image field of view (FOV) of 4′27×4′27. The observing strategy was a 5-point dithering pattern. Given the elongated morphology of the target we used a E-W offset three times larger than that used along the N-S direction.

The data were processed with the package *lirisdr* developed by the LIRIS team within the IRAF environment[1]. The reduction process includes sky subtraction, flat-fielding, correction of geometrical distortion, and finally a combination of frames using the common "shift-and-add" technique. This final step consists of

Table 1. Log of the observations.

Filter	$\lambda_c/\Delta\lambda$ (μm)/(Å)	Date 2006/07/	t_{DIT} (s)	t_{exp} (s)	Seeing (arcsec)
[Fe II]	1.644/280	15	100	2000	1.05
		18	100	600	0.78
		20	60	1800	0.70
H$_2$ υ = 1–0 S(1)	2.122/320	15	100	2000	1.03
		18	10	200	0.65
		20	30	1800	0.78
H	1.625/3100	15	5	500	1.13
K_c	2.270/350	15	100	2000	1.05
		18	20	200	0.75
H_c	1.570/260	18	50	500	0.85

dedithering and co-adding frames taken at different dither points to obtain a mosaic for each filter. The resulting mosaic covers a FOV of ~5 arcmin^2 (see Fig. 1). Note that narrow-band images taken with LIRIS are commonly affected by fringing. An efficient method to correct this effect is to create a superflat image by a median combination of all frames corresponding to a filter and rejecting pixels that contain bright stars.

Continuum-subtracted images of the emission in the [Fe II] and H$_2$ lines were obtained by removing the off-line emission using the images acquired through the H_c and K_c filter respectively. For each pair of H and K images, a flux scaling factor was derived by comparing the counts of several stars in both images and then subtracting the registered and scaled images. In some cases the images with best seeing were degraded by convolution with a Gaussian in order to match the width of the point spread function (PSF).

The astrometric calibration of each final image was made with the aim of properly comparing the structures at near-infrared and optical wavelengths, and with the position of the radio continuum sources found in the field. To do that, the near-infrared images were registered using the coordinates from the 2MASS All Sky Catalogue of ten field stars that are well distributed over the observed field. The rms of the transformation was 0″04 in both coordinates.

In order to estimate the brightness of the detected emission-line structures we determined a photometric zero point for each filter. For this purpose we obtained instrumental magnitudes in each of the final images by using the image-analysis tools of the GAIA interface facility[2]. Firstly, stars in the images were detected with the task *object detection* and then the zero-point was determined through a comparison with the magnitudes from the 2MASS catalogue. The accuracy reached was better than 0.1 mag in all the filters. The limiting magnitudes (at a 3σ level) found for our images were 20.5 mag arcsec^{-2} in H_c and 18.5 mag arcsec^{-2} in K_c. Conversion from magnitude to flux density was made by using the flux of Vega, which was properly interpolated taking into account the narrow-band filter response. Then, the flux was measured for each substructure that could be isolated within the nebular emission features. We defined an ellipse encircling the emission of the substructure to include signal down to a ~3σ limit by means of the *Aperture photometry* task in GAIA (see Figs. 2–4). The background emission was extracted from an ellipse with the same area but encircling a region close to the substructure, which was supposedly free from line emission. For close substructures, which are difficult to isolate, we preferred to enclose them all together within a single ellipse and evaluate the total flux inside. Fluxes are reported in Tables 2 and 3.

---

[1] IRAF is distributed by the National Optical Astronomy Observatories, which are operated by the Association of Universities for Research in Astronomy, Inc., under cooperative agreement with the National Science Foundation.

[2] GAIA is a derivative of the Skycat catalogue and image display tool, developed as part of the VLT project at ESO.
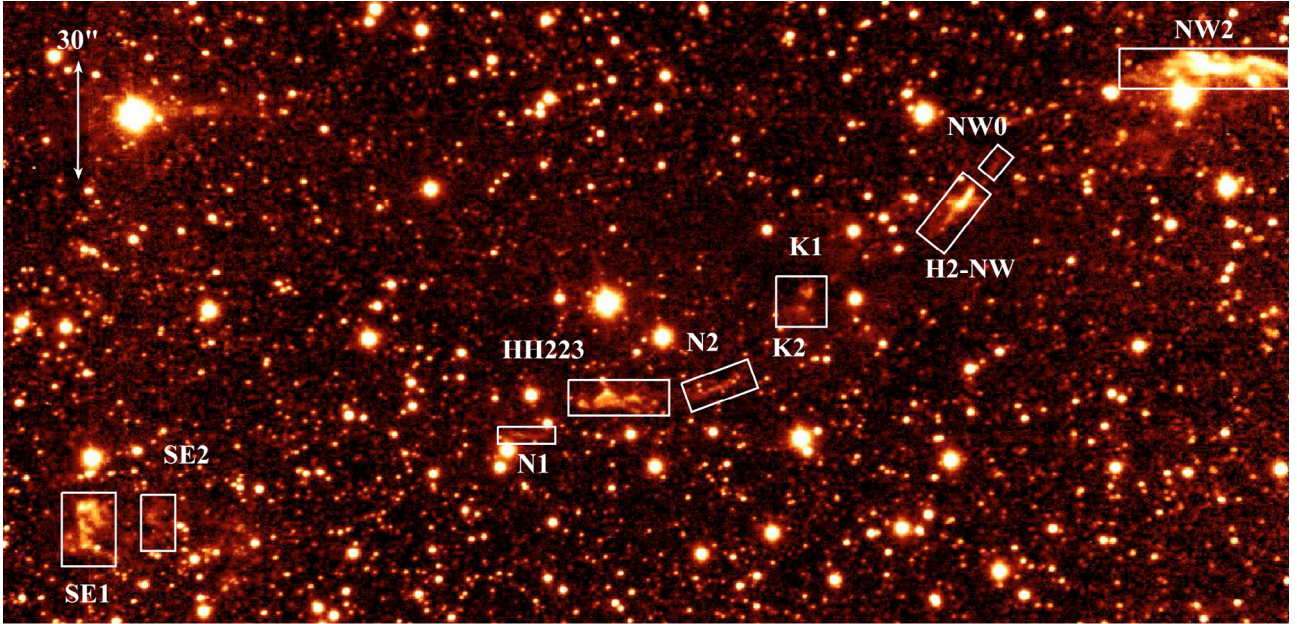
Fig. 1. The L723 field imaged with LIRIS through the H_2 2.122 μm line filter (continuum is not subtracted). The emission structures of the HH 223 outflow have been labeled. North is up and East is to the left.
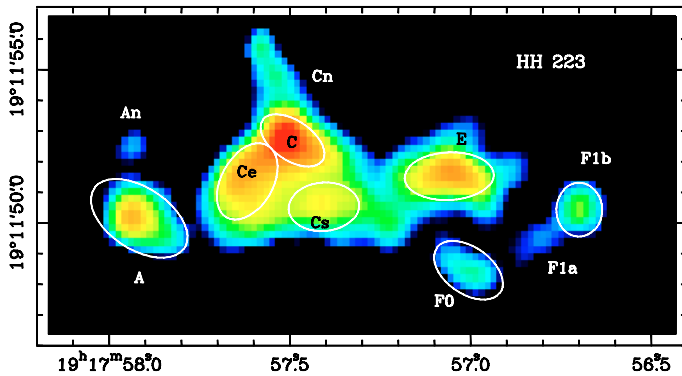
Fig. 2. Close-up of the continuum-subtracted H_2 image showing the structure of the HH 223 emission at the centre of the L723 field. The emission substructures referred to in Col. 1 of Table 2 have been labeled. The white ellipses enclose the regions which correspond to the emission-line fluxes referred to in Cols. 3 and 4 of Table 2.

3. Results

3.1. Outflow morphology in H_2 υ = 1–0

Figure 1 displays an image of the L723 field through the H_2 υ = 1–0 S(1) narrow-band filter that shows the large-scale emission of the HH 223 outflow. As can be seen from the figure, the emission spreads over a length of ~5′.5 (~0.5 pc for a distance of 300 pc) from the southeast to the northwest. It consists of several groups of nebulae of different sizes and complexity, distributed following a S-shaped pattern that lies projected onto the lobes of the east-west CO outflow. The morphology outlined at large scale is then suggestive of a parsec-scale H_2 outflow.

The large-scale morphology of the H_2 emissions agrees well with that of the atomic ($H\alpha$, [S II]) emissions in the loci where both optical and near-infrared emissions are detected. We found the H_2 counterparts of the $H\alpha$ nebulae HH223-SE1, -SE2, -N1, -N2, and of the largest emission, HH 223 (López et al. 2006). Additional H_2 emission nebulae without visible counterpart appear towards the northwest of HH 223. Some of them were previously detected by Palacios & Eiroa (1999) (e.g. labeled in
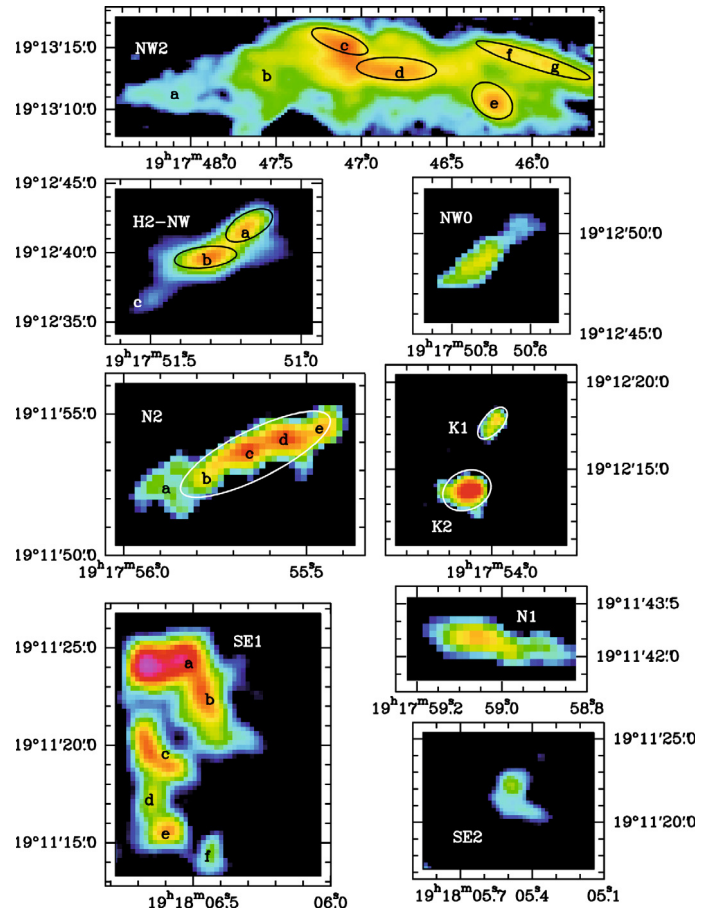
Fig. 3. Close-up of the continuum-subtracted H_2 image showing the other H_2 line-emission nebulae of the HH 223 near-infrared flow (see Table 2 for identification). The ellipses are the same as in Fig. 2.

their work as K1, K2 and H_2-NW). Our new images give a wider coverage of the HH 223 near-infrared outflow. They include new faint emissions (e.g. HH223-NW0, towards the northwest of the field) and the filamentary emission K' reported by
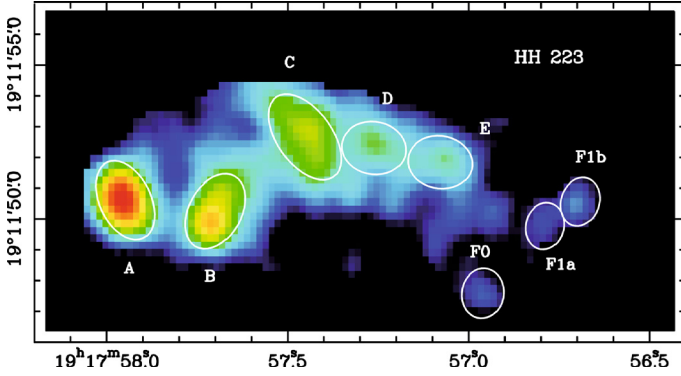
Fig. 4. Close-up of the continuum-subtracted [Fe II] image showing HH 223. The knotty substructures referred in Table 3 have been labeled on the figure. The ellipses are the same as in Figs. 2 and 3.

Hodapp (1994), which has a Hα counterpart (HH223-NW2) weaker and less extended. In addition, we were able to distinguish the emission contributions from the continuum and from the H_2 line. The continuum-subtracted H_2 image shows several emission spots that appear to be extended nebulae surrounding embedded stars, whose physical association with the stars cannot be established from the present data. In contrast, most of the filamentary emission features come from "true" line emission that appear complex and knotty, with several condensations embedded inside a more diffuse nebular emission.

The "true" H_2 line emission nebulae along the HH 223 near-infrared outflow were identified from the continuum-subtracted H_2 image, and those with a spatially-extended structure have been resolved in smaller substructures. In this work, the H_2 nebulae have been labeled according to the nomenclature of Palacios & Eiroa (1999), but we expanded it with the newly found near-infrared features. There is an exception concerning to the emission of ~30″ length towards the centre of the field (i.e. HH 223), where we keep the nomenclature established in López et al. (2006) for the Hα and [S II] knots. Similar to what we did for the Hα and [S II] line-emission features, we added the identification label *HH 223-* to all the H_2 nebulae found projected onto the east-west CO outflow, since they most probably form part of the same near-infrared/optical outflow.

The H_2 emission structures identified from our image are listed in Table 2 (Col. 1), and their positions are given in Cols. 2 and 3. The H_2 line flux of the nebulae, integrated over the area of Col. 4, is given in Col. 5. Figure 2 displays a close-up of HH 223, showing the morphology of the H_2 emission with detail. Figure 3 shows close-up of several extended nebulae (those containing smaller substructures) along the HH 223 near-infrared outflow.

We will briefly describe the main emission nebulae below, beginning with HH 223. The rest of H_2 emission nebulae are listed from southeast to northwest.

HH 223: the knotty, undulating structure of ~22″ in length found towards the centre of the field, ~1′ southeast of the radio continuum system VLA 2. The H_2 feature spatially coincides with the Hα "linear emission feature" reported by Vrba et al. (1986), which corresponds to HH 223 in the Reipurth Catalogue of Herbig-Haro objects (Reipurth 1994). Part of this structure (from HH 223-C to HH 223-F) corresponds to the H2-SE emission of Palacios & Eiroa (1999). The field imaged by these authors covers up to the eastern edge of HH 223-C, so that HH 223-A was not mapped. Since the overall morphology and size of HH 223 is similar for the optical and near-infrared emissions and to facilitate the

comparison between them, we adopt the nomenclature for the knots of López et al. (2006), instead of using the H2-SE label given in Palacios & Eiroa (1999) for the part of the H_2 emission mapped by them. In spite of the similarity between the optical and near-infrared emissions, a more detailed comparison shows differences that will be discussed later.

HH 223-SE1 -SE2: a group of H_2 nebulae ~2′ southeast of HH 223-A, the counterparts of the Hα nebulae HH 223-SE1 (also associated with the V83 nebula of Vrba et al. 1986) and HH 223-SE2, reported by López et al. (2006). HH 223-SE1, unresolved in Hα, consists of several arc-shaped structures of different sizes (SE1-a to -f) in the H_2 image. HH 223-SE2 appears in H_2 as a faint, bow-shaped structure (labeled SE2 in Table 2 and Fig. 3).

HH 223-N1: faint, filamentary S-shaped emission that extends over ~11″ in length, ~15″ southeast of HH 223-A. Only the brightest eastern part of it, of ~5″ in length was barely detected in Hα.

HH 223-H2-N2: faint filamentary H_2 feature ~30″ northwest of HH 223-A and extending over ≈15″ towards the northwest, projected onto the blueshifted CO outflow lobe. This emission was barely detected in the image of Palacios & Eiroa (1999). Our H_2 image shows several brightness emission enhancements (labeled -b to -e in Table 2 and Fig. 3). No visible counterpart was detected for this emission, except for its faint eastern part (H2-N2-a), which coincides with the Hα emission HH 223-N2.

HH 223-K2, -K1: these two emission nebulae, ~60″.5 (K2) and ~64″ (K1) northwest of HH 223-A, are the nebulae closest to the radio continuum multiple system VLA 2. They were first reported by Palacios & Eiroa (1999) as two low-brightness H_2 patches. K2 appears in our images as a quite compact knot of ~3″ in diameter. Its emission mostly arises from the H_2 line, as shown in the H_2 continuum-subtracted frame (see panels in Figs. 2 and 8). The emission of K1 has contributions from both continuum and line. In the the H_2 continuum-subtracted frame, K1 shows an elongated shape extending ~3″ along a direction with a position angle ~130° (see panel of Fig. 2). In contrast its morphology is somewhat different in the H_2 frame keeping the continuum: the K1 emission extends in an emission tail towards its eastern side and, in addition, K1 appears brighter than K2.

HH 223-H2-NW, -NW0: HH 223-H2-NW is the emission of ~12″ length, found ~1′.5 northwest of HH 223-A. Its shape follows a smooth undulating pattern, with at least three substructures enclosed in a more diffuse emission. North of HH 223-H2-NW, an additional filamentary emission of ~2″ length has been detected in our images. It has been labeled HH 223-NW0 to distinguish it from the rest of the HH 223-NW emissions found in the Hα and H_2 images, which are located few arcmin from HH 223.

HH 223-H2-NW2: the bright, filamentary H_2 emission, with several substructures inside, which is seen towards the northwestern edge of the field. The emission coincides with a K' linear nebula reported by Hodapp (1994). Part of the HH 223-H2-NW2 structure is the counterpart of the faint Hα nebula HH 223-NW2.

3.2. [Fe II] imaging

Additional images of the L723 field were obtained in the *H*-band (see Table 1). After subtracting the H_c from the [Fe II] + continuum images, significant emission from the [Fe II] line was only detected at the location of HH 223. The structure of the [Fe II] emission consists of several knotty condensations inside

Table 2. Positions and photometry of the H_2 features detected in the L723 field.

| | Peak Position | | Photometry | | |
| | α_{2000} | δ_{2000} | Integrated area | H_2 line flux | |
H_2 feature	(h m s)	(° ′ ″)	(arcsec^2)	(10^{-15} erg cm^{-2} s^{-1})	Notes
SE1 (V83) region					(1),(4)
a	19 18 06.63	+19 11 24.6			
b	19 18 06.47	+19 11 23.0			
c	19 18 06.65	+19 11 19.3			
d	19 18 06.67	+19 11 17.1			
e	19 18 06.61	+19 11 15.4			
f	19 18 06.44	+19 11 14.0			
SE2	19 18 05.48	+19 11 22.1			(1),(4)
N1	19 17 59.04	+19 11 42.3	3.77	0.51 ± 0.08	(1),(5)
HH 223					(2),(6)
An	19 17 57.96	+19 11 52.5			(3)
A	19 17 57.96	+19 11 50.1	7.30	4.16 ± 0.13	(2)
Cn	19 17 57.55	+19 11 54.8			(3)
Ce	19 17 57.64	+19 11 51.1	4.68	6.85 ± 0.10	(3)
C	19 17 57.51	+19 11 52.8	3.14	5.58 ± 0.07	(2)
Cs	19 17 57.42	+19 11 50.6	3.74	2.78 ± 0.10	(3)
E	19 17 57.04	+19 11 51.5	4.64	4.04 ± 0.12	(2)
F0	19 17 56.98	+19 11 48.0	3.94	0.85 ± 0.07	(2)
F1a	19 17 56.78	+19 11 49.3			(2)
F1b	19 17 56.67	+19 11 50.3	2.69	1.26 ± 0.08	(2)
H2-N2			10.32	0.59 ± 0.15	(1),(7)
a	19 17 55.87	+19 11 52.3			
b	19 17 55.78	+19 11 52.6			
c	19 17 55.66	+19 11 53.8			
d	19 17 55.55	+19 11 54.2			
e	19 17 55.42	+19 11 54.6			(3)
K2	19 17 54.10	+19 12 13.6	7.15	1.54 ± 0.11	(3)
K1	19 17 53.96	+19 12 18.1	2.81	0.53 ± 0.07	
H2-NW					(3)
a	19 17 51.17	+19 12 42.0	4.24	12.6 ± 0.10	
b	19 17 51.30	+19 12 39.6	4.23	14.2 ± 0.08	
c	19 17 51.51	+19 12 36.3			
H2-NW0	19 17 50.68	+19 12 49.1			(8)
H2-NW2					(9)
a	19 17 48.11	+19 13 11.4			
b	19 17 47.56	+19 13 14.4			
c	19 17 47.09	+19 13 14.8	7.11	43.4 ± 0.16	
d	19 17 46.80	+19 13 13.1	11.51	37.3 ± 0.19	
e	19 17 46.20	+19 13 10.3	8.97	33.8 ± 0.21	
f	19 17 46.11	+19 13 15.0	11.75	17.3 ± 0.22	(10)
g	19 17 45.88	+19 13 13.6			

Notes. (1) With counterpart in Hα; (2) with counterpart in Hα and [S II]; (3) without optical counterpart; (4) position of the apex; (5) position of the peak intensity; (6) this emission has been labeled as its optical counterpart; the region between knots C and F corresponds to the H_2 emission labeled as H2-SE by Palacios & Eiroa (1999); (7) knots b to e have been included in the flux value; (8) first detection in this work; (9) weak Hα counterpart; detected in K' by Hodapp (1994); (10) knots f and g have been included in the flux value.

Table 3. Positions and photometry of the [Fe II] features detected in the L723 field.

| | Peak Position | | Photometry | |
| | α_{2000} | δ_{2000} | Integrated area | [Fe II] line flux |
[Fe II] feature	(h m s)	(° ′ ″)	(arcsec^2)	(10^{-15} erg cm^{-2} s^{-1})
HH 223[1],[2]				
A	19 17 57.99	+19 11 50.4	4.68	5.95 ± 0.10
B	19 17 57.73	+19 11 49.7	4.58	3.39 ± 0.10
C	19 17 57.45	+19 11 52.9	5.83	3.64 ± 0.09
D	19 17 57.26	+19 11 52.2	3.68	1.16 ± 0.09
E	19 17 57.05	+19 11 51.8	3.68	0.71 ± 0.07
F0	19 17 56.96	+19 11 47.2	2.28	0.14 ± 0.25
F1a	19 17 56.77	+19 11 49.6	1.94	0.28 ± 0.06
F1b	19 17 56.68	+19 11 50.3	2.18	0.37 ± 0.07

Notes. (1) The knots were labeled as its optical counterparts. Knot B has not been detected in H_2; (2) note the displacements between the [Fe II] and H_2 emission peak positions (see text).
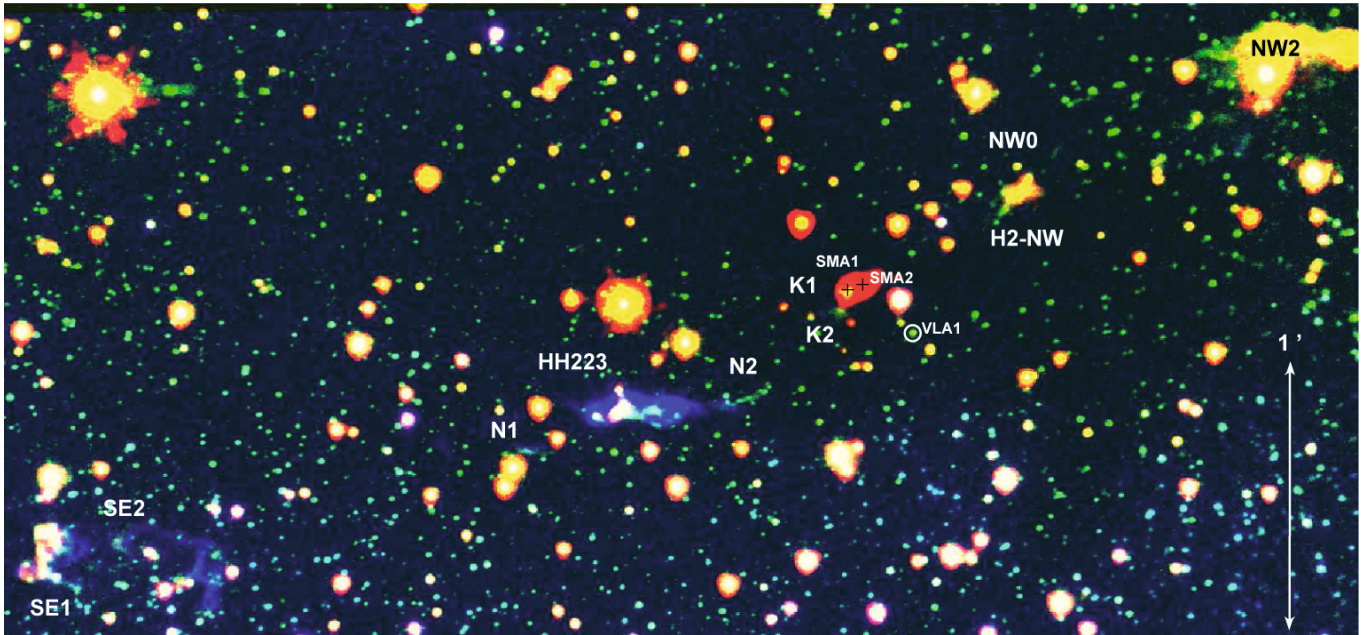
Fig. 5. Composite image of the L723 field using a Hα (blue), H_2 2.122 μm (green) and IRAC 4.5 μm (red) colour coding to show the HH 223 outflow emissions. The positions of the radio continuum sources SMA1 and SMA2 have been marked by plus signs. The near-infrared counterpart of the radio source VLA 1 has been marked by a circle. The continua were not subtracted to facilitate the alignment of all images using the field stars.

a lower-brightness nebular emission (see Fig. 4). In Table 3 we list the [Fe II] condensations of HH 223 (Col. 1), their peak position coordinates (Cols. 2, 3) and the [Fe II] line flux (Col. 5), integrated within the area given in Col. 4. As can be seen from the figure, the [Fe II] emission of HH 223 extends from east to west over a similar length than the emissions in the H_2 and Hα lines. The overall morphologies are also similar. However, some significant differences are found when these emissions are compared in detail. We will discuss this point in the next section.

Emission from the [Fe II] line was not detected out of HH 223. Emission from this line has been frequently found close to the location of embedded young stellar objects (YSOs), and traces the innermost part of the jet that is accelerated near the driving source (see, e.g. Reipurth et al. 2000). Hence, one would expected to find [Fe II] emission associated with K1, the H_2 nebula found closest to the radio continuum system VLA 2. However, no emission was detected in our images around K1. Likely, the extinction is high enough to prevent the detection, provided that the degree of ionization of the outflow is low enough to produce only faint [Fe II] emission.

It is not reasonable to expect emission from the [Fe II] line at regions having Hα emission and no counterpart in the [S II] lines (like HH 223-SE or HH 223-NW2). This is because of the 1.644 μm [Fe II] and [S II] lines arise from similar excited atomic levels, and both species have similar ionization potentials.

4. Discussion

4.1. Comparing the optical and near-infrared emissions of the HH 223 outflow

It is interesting to compare the morphology of the HH 223 outflow emission for different spectral ranges. This can be done from the available images of the the L723 field that include the outflow.

At optical wavelengths, we use the deep narrow-band Hα and [S II] images acquired with the 2.6-m Nordic Optical Telescope (NOT) (see López et al. 2006, for details of the

observations). In addition to the near-infrared images in the *H* and *K* bands discussed in this work, we use an image of the Spitzer Infrared Array Camera (IRAC) through its channel 2 (centred at 4.5 μm). For the typical conditions of low-mass outflows, emission from several rotational transitions lines of H_2 should be expected within the ≈4–8 μm wavelength range. It is well-known that the IRAC channel 2 is the best suited in detecting shock-excited H_2 features, in contrast with the IRAC channels 3 (5.8 μm) and 4 (8.0 μm). This is because channel 2 is the band that is less contaminated by extended emission arising from polycyclic aromatic hydrocarbon (PAH). The IRAC channel 2 image of the L723 field was obtained from the Spitzer Science Archive using the Leopard software. The image used here corresponds to the post-basic calibrated data (pbcd) obtained in the project P00139 *From Molecular Cores to Planet* (PI N. Evans).

The original images of the bands we compared have a different spatial scale and FOV. In order to do more meaningful comparisons, all images were transformed to reach the same magnification. First, we extracted a subimage of the IRAC frame after rotating the original pbcd frame by the appropriate angle to be oriented in the standard way. Then, we identified six stars that are common to all images and are well distributed in the field. These stars were used to register the images for converting all of them into a common reference system with the IRAF tasks GEOMAP and GEOTRAN. All the final five frames (i.e. Hα, [S II], [Fe II], H_2 at 2.122 μm and at 4.5 μm) used here to compare the HH 223 outflow emissions have a spatial scale of 0.″6 pixel^{-1}.

4.1.1. Atomic and molecular hydrogen emissions

Figure 5 displays a composite image of the L723 field, where the emission from atomic (Hα) and molecular (H_2 2.122 μm and 4.5 μm) hydrogen lines appear superposed. The figure reveals that the large-scale morphology of the HH 223 outflow is very similar. However, slight differences in several structures can be appreciated when the hydrogen emission from each band is compared in detail.

The HH 223-SE1, SE2 and N1 nebulae at the southeastern side of the HH 223 outflow are detected in the three bands, and they are spatially coincident. However, HH 223-SE2 shows a bow-shaped morphology in the two H_2 emission bands, while this shape is not as clearly outlined in Hα, where the emission appears more extended and filamentary.

To the northwestern side of the outflow, the HH 223-H2-NW and H2-NW2 nebulae appear bright and with a very similar morphology in the two H_2 emissions, while in Hα H2-NW was undetected, and H2-NW2 was barely detected and appears shorter. These differences could be due to the extinction, since both structures are located within a region that appears highly obscured at optical wavelengths.

The faint filamentary feature HH 223-N2 detected at 2.122 μm has neither Hα nor 4.5 μm counterparts. The lack of Hα emission a this location should be expected because of the high visual extinction. In contrast, we believe that the lack of counterpart at 4.5 μm might be better attributed to the weakness of the emission, which is below the detection limit of the IRAC frame.

HH 223, at the centre of the field, shows a morphology and a spatial brightness distribution closely coincident for the emissions in molecular hydrogen at 2.122 μm and 4.5 μm. Some differences appears however when the H_2 and Hα emissions are compared in detail. One difference is that the low-brightness emission surrounding the knots appears more extended in Hα than in H_2. The knots appear better delimited, with their edges sharper in Hα than in H_2. Another more relevant difference is the lack of counterparts in H_2 for knot B, which is very bright in Hα, and for knot D, which cannot be resolved as a knotty structure within the low-brightness emission, in contrast to what happens in Hα. Finally, several faint knotty structures were identified in the H_2 2.122 μm line without a counterpart in Hα (i.e. those labeled An, Cs, Ce and F0, this last belonging to the F filament). An additional low-brightness filamentary emission in H_2 2.122 μm, without counterpart in Hα, was identified extending ~3″ from knot C to the northeast. The variations of the physical conditions and, in particular, of the gas kinematics through HH 223 seem to be mainly responsible for the differences found between the atomic and the molecular hydrogen emissions. We will return to this point later.

No Hα counterparts were detected at the positions of the HH 223-K1 and K2 nebulae. This should be expected because of the high visual extinction in this region, where the radio continuum sources are located. In contrast, counterparts at 4.5 μm for both HH 223-K1 and K2 are detected in the IRAC frame. Note however that at 2.122 μm the emission of HH 223-K2 appears rather more extended towards the southeast, away from the radio continuum sources, than at 4.5 μm.

Concerning HH 223-K1, the emission appears significantly more extended at 4.5 μm than at 2.122 μm. The emission at 4.5 μm spreads towards the northwest, beyond its counterpart at 2.122 μm, and encompasses the region where the two radio continuum sources (SMA1 and SMA2) are located. In contrast, as can be seen in Fig. 5, the emission of K1 at 2.122 μm does not reach the position of SMA2 (see also Fig. 8). The extinction is probably high enough to prevent its detection in the K band around this position. Furthermore, as in the case of the emission associated with K1 in the K band, its counterpart at 4.5 μm could have continuum contribution from heated material of the wall cavity opened by the outflow, which can be traced closer to the radio continuum sources at this wavelength.
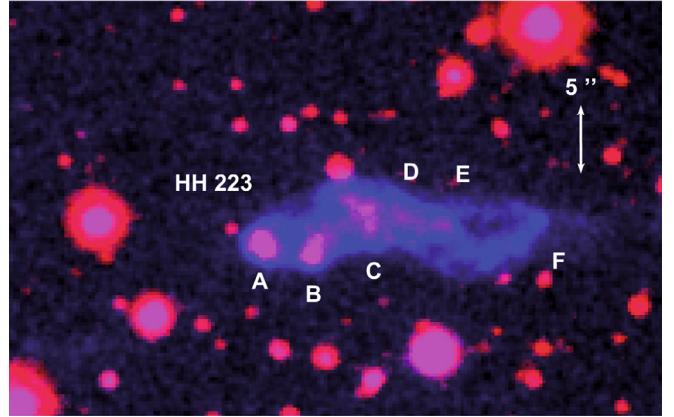
Fig. 6. Composite image of HH 223 using a [S II] 6716,31 Å (blue) and [Fe II] 1.644 μm (red) colour coding (continua were not subtracted). North is up and East is to the left.

4.1.2. [S II] and [Fe II] emissions

The near-infrared [Fe II] 1.644 μm emission, when detected, appear spatially coincident with the [S II] λ 6716, 31 Å emission. Both emissions usually have a very similar morphology (see e.g. Reipurth et al. 2000; Davis et al. 2003). Also, the differences between their detailed structures are much smaller than the differences found between the [Fe II] and H_2 emissions. This is because the [S II] and [Fe II] lines arise from atomic levels of similar excitation energy and ionization potential. Thus, it is expected the emission from both lines to be spatially coincident, tracing the shock-ionized gas component of the outflow. However, the relative brightness distribution for both emissions could vary. This is not only owing to differential extinction effects, but also because of the higher [Fe II] critical density ($\simeq$one order of magnitude above the [S II] critical density). Hence, the [Fe II] emission requires a higher pre-shock gas density and/or a faster shock velocity to reach an intensity comparable to the [S II] emission intensity.

Figure 6 shows a close-up of the L723 field including HH 223 from knot A to filament F, where the emissions from [S II] 6716,31 Å (in blue) and [Fe II] 1.644 μm (in red) have been superposed. The knots detected in the [Fe II] line (see also Fig. 4) have the corresponding [S II] knotty counterpart as would be expected, although the knots appear more compact in [Fe II] than in [S II]. Moreover, the emission coming from the lower-brightness nebula surrounding the knots is much fainter in [Fe II] than in [S II].

Some clues on the spatial distribution and on the relative strength of both emissions are obtained from the kinematics and physical conditions through HH 223, derived in López et al. (2009) from long-slit optical spectroscopy.

For example, the line-ratio diagnosis shows that knot A (one of the brightest in [Fe II]) is the densest, most excited and highly ionized knot (indeed, the electron density derived at several positions inside knot A fall above the [S II] critical density for collisional de-excitation). In contrast, the electron densities derived in the low-brightness nebula as well as in the fainter HH 223 knots (D to F), are up to one order of magnitude lower. In addition, the excitation and ionization measured in these knots (D to F) are visibly lower than in knot A. Hence, the excitation and density conditions in knot A could explain its high [Fe II] emission as compared with the rest of the knots. This is consistent with the results derived by Nisini et al. (2002) and Nisini et al. (2005) in several HH objects with a more accurate diagnostic
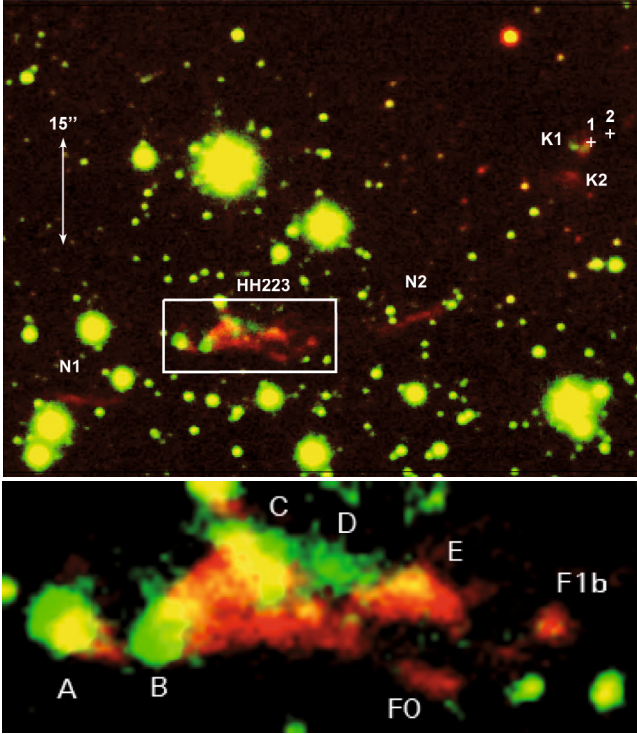
Fig. 7. *Top panel*: Composite image, using a H$_2$ 2.122 μm (red) and [Fe II] 1.644 μm (green) colour coding, of a FOV ~1'.5 × 1'.1 of L723 showing part of the HH 223 outflow (continua were not subtracted). Crosses mark the position of the radio continuum sources SMA1 and SMA2, close to the H$_2$ structure K1 (see also Fig. 8). *Bottom panel*: Close-up of the ~24'.3 × 10'.2 rectangle enclosing HH 223. Note the spatial displacements between the [Fe II] and H$_2$ emissions in the knots. North is up and East is to the left.

from combined optical/near-infrared spectroscopy. These authors were able to detect a density stratification from ratios of forbidden lines with different critical densities (such as [S II] and [Fe II]) as well as variations of the spatial distribution of the ionization/excitation conditions along the jet emission. In particular, they derived that the [Fe II] emission comes from the densest and/or highly ionized jet regions.

On the other hand, note that knot B is bright in [Fe II], but lacking of apparent emission in H$_2$. Knot C, detected in H$_2$, has a [Fe II] emission weaker than knot B. Concerning their conditions, from the optical spectra we derived very similar electron densities and excitation/ionization degrees for knots B and C. In contrast, knot B is one of the faster HH 223 knots. The radial velocity derived for knot B ($V_{LSR} = -125$ km s^{-1}) is appreciably higher (by a factor of two) than for knot C ($V_{LSR} = -55$ km s^{-1}). Thus, we interpret that the discrepancies found between the [Fe II] and [S II] emissions are more likely produced by the kinematics and physical conditions in the knots than by differential extinction effects: knots denser and/or faster are stronger emitters in the [Fe II] line than slower and/or more rarefied knots. Furthermore, the emission appears spatially more extended in [S II], which gives rise to an extended low-brightness nebula around the knots, than in [Fe II]. This could be explained because we are detecting [Fe II] emission only from the higher density material of the knots. Thus, the shape of the overall [Fe II] emission appears more compact than the [S II] emission. The lack of detection of the H$_2$ line coinciding with the position of the fastest knot B also supports this interpretation, since the dissociation of the H$_2$ molecule can be more efficient at the knots with higher velocity.

4.1.3. [Fe II] and H$_2$ ν = 1−0 S(1) emissions

Usually, the H$_2$ and [Fe II] emissions from jets show different spatial brightness distributions: the H$_2$ emission is more diffuse and extended than the [Fe II] emission (see e.g. Reipurth et al. 2000). Here we will compare in greater detail the emission from both species in the HH 223 outflow. Figure 7 displays a composite image, where the emissions from [Fe II] 1.644 μm (in green) and H$_2$ 2.122 μm (in red) appear superposed.

Several differences between the spatial brightness distribution of these two emissions are appreciated. First, the shape of some knots is different. This is clearly seen e.g. for knot E. The emission of this knot appears more extended in H$_2$ and shows a bow-shaped morphology as compared to [Fe II], where the emission is more compact. Second, the relative intensity between the knots is also different. Note, e.g. that knots A and C show a similar brightness in H$_2$, while knot C appears appreciably weaker in the [Fe II] line compared to knot A. Even more noticeable is the lack of H$_2$ emission at the position of knot B, which is one of the brightest in [Fe II]. Finally, we obtained reliable measurements of the position offsets between the [Fe II] and H$_2$ emission intensity peaks: in knot A the [Fe II] emission peaks ~0'.7 northeast of the H$_2$ emission peak; in knot C the [Fe II] peak is ~1'.1 northwest of the H$_2$ peak (see also Fig. 7, bottom panel).

Again, we interpret these differences between both emissions as mostly caused by the excitation conditions required for each line to emit, namely shock velocity and gas density, rather than to differential extinction effects. Further support of this interpretation comes from the anticorrelation that we found between the radial velocities of the knots in HH 223, derived from optical spectroscopy, and their relative H$_2$ brightness. The radial velocity decreases for the sequence of knots B, D, A, E and C, while the H$_2$ brightness increases for the sequence of knots C, E, A; the emission is very weak in D and is below detection limit in knot B where, in addition, the degree of ionization inferred from optical line ratios reaches the lowest value measured in all knots.

As mentioned before, [Fe II] line emission was only detected associated with HH 223. The *H*-band emission detected around the location of K1, the H$_2$ nebula closest to the radio continuum sources, mainly arises from continuum.

Some of the lower-brightness diffuse H$_2$ emission features without [Fe II] counterpart may trace slower shocks in the ambient molecular gas with which the supersonic jet is colliding. This was suggested to explain the nature of the H$_2$ emission structures lacking of [Fe II] counterpart that, as in our case, were detected along the molecular outflow lobe associated with the jet powered by L1551 NE (Hayashi & Pyo 2009).

4.2. Near-Infrared environment of the radio continuum multiple system VLA 2

Figure 8 displays a close-up of L723 dark cloud showing the field around the low-mass protostellar multiple system (VLA 2A to 2D) embedded in the region. The panels of the Fig. 8 display the near-infrared emission in the *H* and *K* bands obtained from the images of this work.

As mentioned before, Palacios & Eiroa (1999) reported the detection of two faint H$_2$ nebulae, named K1 and K2, near VLA 2. However, our images indicate that the nature of the emission is different for K1 and K2.

Concerning K1, our images indicate that its emission has contributions from both line and continuum. This can be seen in the panels of Fig. 3 and its comparison with Fig. 8. The morphology of K1 both in the *H* and *K* band images including continua consists of a nearly arc-shaped nebula, with two
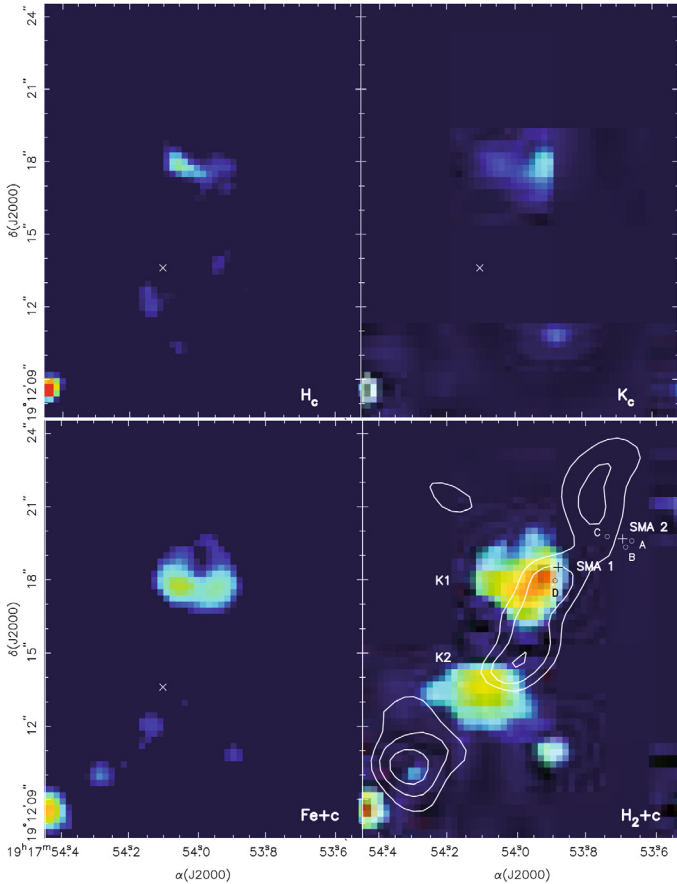
Fig. 8. Close-up of the L723 field including the K2 and K1 near-infrared structures, in the neighbourhood of the radio continuum multiple system VLA 2. In the lower-right panel, the crosses mark the positions of the sources SMA1 and SMA2 detected at 1.35 mm by Girart et al. (2009). The circles mark the positions of the four components of VLA 2 (i.e. VLA 2A to D) detected at 3.6 cm and 7 mm by Carrasco-González et al. (2008). The SiO outflow reported by Girart et al. (2009) has been superposed on the image with white contours. The position of the H_2 emission peak of K2 has been marked with a tilted cross in the other three panels.

(east and west) brightness enhancements of different intensity. The emission of the [Fe II] 1.644 μm line falls below the detection limit, as revealed from the continuum-subtracted [Fe II] image. The emission from the H_2 2.122 μm line only contributes to the western part of K1 (the side closer to the radio continuum sources) and appears elongated in the northwest-southeast direction (PA $\simeq$ 140°). Interestingly, Girart et al. (2009) reported emission of the SiO 5–4 line towards the position of the radio continuum sources. The SiO emission shows an elongated morphology, reminiscent of a jet, which also follows the northwest-southeast direction. Moreover, the H_2 emission peaks of K1 and K2 are in good coincidence with two SiO emission enhancements (note that the positions of knots K1 and K2 in Fig. 6 of Girart et al. (2009) are offset ~5″ east of the position reported in this work). The SiO line is a tracer of shock-excited molecular gas. Hence, it seems reasonable to assume that both emissions, H_2 2.122 μm and the SiO, are tracing the same outflow. The continuum emission from the eastern side of K1 may arise from heated material of a cavity wall.

Concerning K2, which lies south of the radio continuum system, the near-infrared emission in the H_c and K_c (continuous) bands falls below the detection limit. In contrast K2 appears quite bright, with a magnitude of 17.3, in the H_2 narrow-band

image, and remains without appreciable differences after subtracting the continuum, both in shape and brightness. Hence, K2 emission comes mostly from the 2.122 μm line, which is tracing shock-excited gas (note that excitation by fluorescence cannot be a likely option because of no ionization sources, like early-type stars, are found associated with the L723 dark cloud). Interestingly, another clump of SiO emission is detected ~6″ southeast of the K2 intensity peak. This clump is aligned with the CO outflow direction. This reinforces the idea that the near-infrared (H_2 line) and SiO emissions are tracing shock-excited gas in a jet, and points towards SMA1 as the likely source powering the SiO outflow.

4.3. The nature of the radio continuum source VLA 1

Anglada et al. (1991) detected at 3.6 cm another radio continuum source, VLA 1, located ~15″ southwest of VLA 2. Later radio observations by Anglada et al. (1996) and Girart et al. (1997) led to discard VLA 1 as a young stellar object (YSO) associated with the CO multipolar outflow. As discussed by Girart et al. (2009), VLA 1 is not associated with the high-density molecular gas, lying outside, near the border, of the NH_3 structure encompassing the radio continuum system VLA 2, and suggest that VLA 1 is a line-of-sight radio source unrelated to the outflow. However, the nature of the radio source VLA 1 has not been settled up to date. Carrasco-González et al. (2008) reanalyse multiepoch, centimetre and millimetre data of L723. Their data are compatible with VLA 1 belonging to the L723 cloud and being a radio-emitting, optically obscured T-Tauri star.

Interestingly, we found in all our *H*- and *K*-band images a stellar-like, near-infrared counterpart with coordinates α = $19^h17^m52^s.93$, δ = $+19°12'8''.8$, which coincided within 0″.05 with the position of VLA 1 (Carrasco-González et al. 2008). This counterpart (see Fig. 5) is also detected in the four IRAC channels (3.6, 4.5, 5.8, and 8.0 μm) of the Spitzer images mentioned in Sect. 4. We performed aperture photometry of the VLA 1 near-infrared counterpart for all the detected bands and found magnitudes of 18.6, 17.0, 15.0, 14.9, 14.8, and 14.8 in the Hc, Kc, 3.6, 4.5, 5.8, and 8.0 μm images, respectively (errors in magnitude are estimated to be $\leq$ 0.1 mag). All magnitudes were calibrated relative to Vega (see e.g. Reach et al. 2005, for IRAC). We combined these data to obtain near-infrared colours for the VLA 1 counterpart. Following the current classification criteria (see e.g. Fang et al. 2009, and references therein), we found that the colours of this source are consistent with those of an evolved YSO of Class III. In particular, the position of this source in the [5.8]–[8.0] vs. [3.6]–[4.5] colour diagram corresponds to the loci where the Class III YSOs are located, and is also compatible within the errors with the loci of the transition disc sources. In contrast, the VLA 1 counterpart lies outside the diagram region where the background extragalactic sources are located. From these data we conclude that VLA 1 is tracing the emission of an evolved pre-main sequence star of L723, as proposed by Carrasco-González et al. (2008). However, VLA 1 is likely unrelated to the molecular outflows of L723, because the powering sources of these outflows need to be YSOs in an earlier evolutionary stage than Class II/III.

5. Summary and conclusions

We present near-infrared images of the L723 field, obtained with narrow-band filters centred on the [Fe II] λ 1.644 μm and H_2 v = 1–0 S(1) lines, together with the off-line filters H_c and K_c. The images cover an area of 4′.3 × 4′.3, thus include all the line-emission nebulae associated with the HH 223 outflow that

were detected in Hα. The analysis of the near-infrared images lead us to the main results summarized below.

1. We detected H$_2$ emission in a set of elongated nebular structures that appear distributed from the southeast to the northwest of the L723 field, extending $\sim$5$'$5 ($\sim$0.5 pc for a distance of 300 pc), which is reminiscent of a parsec-scale outflow. The H$_2$ structures are found projected on the lobes of the larger, east-west CO outflow, with an S-shape morphology. Several H$_2$ structures are new identifications from this work.

2. Additional off-line filter images revealed that there is no significant contribution from the continuum to the emission of the nebular structures detected in the K band, except in HH 223-K1, the structure closest to the position of the radio continuum system VLA 2.

3. Emission from the [Fe II] 1.644 μm line was only detected in HH 223 at the centre of the imaged field. Additional significant emission in the H band, which mainly arises from continuum, was detected in HH 223-K1.

4. We compared the appearance of the HH 223 outflow in the optical (Hα and [S II] lines) and near-infrared ([Fe II] at 1.644 μm, and H$_2$ at 2.122 μm at 4.5 μm) wavelength ranges, looking for the nature of the emissions.

   – In general, the HH 223 outflow shows a similar large-scale morphology when the emissions from molecular (at 2.122 and 4.5 μm) and atomic (Hα) hydrogen lines are compared. Some of the discrepancies found among the three bands could be attributed to extinction effects (e.g. the non detection of Hα counterpart from the near-infrared nebulae close to the radio continuum multiple system VLA2, and the larger extension of the 4.5 μm emission compared with the emission at 2.122 μm, in HH 223-K1). Other discrepancies are better explained from the physical conditions and kinematics of the region where they appear: e.g. the non detection of an H$_2$ counterpart for the Hα emission at HH 223-B.
   – The [S II] and [Fe II] emissions are well coincident for all the knots of HH 223 (the only structure of the outflow where near-infrared, line-emission from ionized gas was detected). The low-brightness emission surrounding the knots is more extended in [S II] than in [Fe II]. We attribute this to the lower velocity and density found around the knots, which is unable to excite the [Fe II] emission.
   – Some differences are found when the [Fe II] and H$_2$ 2.122 μm emissions are compared. The differences can be better attributed to the different physical conditions required for these lines to emit (e.g. velocity and density) than to be caused by extinction.

5. We identified the near-infrared counterpart of the radio source VLA 1 in the H, K and the four IRAC bands. The position of this source in the colour-colour diagrams indicates that VLA 1 is tracing the emission of an evolved (Class III) YSO. Thus, VLA 1 is likely unrelated to the H$_2$ outflow.

6. Finally, we discussed the nature of the near-infrared emission for the nebulae closest to the radio continuum sources, which is a candidate to power the molecular and optical outflows. We propose that the H$_2$ 2.122 μm emission in HH 223-K1 and K2 is tracing shock-excited outflow gas, which also was detected in SiO (Girart et al. 2009), because the emission peaks of the K1 and K2 near-infrared structures are coincident with two enhancements of the SiO emission. In addition both H$_2$ and SiO emissions appear elongated along a similar direction (PA $\sim$ 140°). The extended continuum emission

associated with HH 223-K1 could be tracing the walls cavity opened by the outflow.

In summary, we propose that the H$_2$ nebular structures detected in the L723 dark cloud are most probably associated with the radio continuum system of protostellar sources found in this dark cloud. All these H$_2$ nebular structures could form part of a S-shaped outflow that also have an optical counterpart in the regions with low visual extinction.

The knotty structures of the HH 223 outflow could be tracing internal working surfaces of shocks that originate because the gas is ejected at varying speeds and/or with a varying direction and faster ejecta overtake slower ones. A variable ejection velocity and an undulating jet morphology is expected when the exciting outflow source belongs to a binary system. The low-brightness, more diffuse line-emission structures could be tracing slow shocks, excited by the interaction of the CO outflow with the accelerated gas of the walls cavity opened by it. The emission from the [Fe II] line could be tracing the densest and high-ionized regions in the outflow.

The current data still do not allow us to discern which of the radio continuum component of the VLA 2 system is powering the large scale, near-infrared/optical HH 223 outflow. However at small scales (i.e. short dynamic time scales), the near-infrared emission and the SiO outflow seem to be powered by SMA1. The large-scale scenario can be better settled by analysing the kinematics and excitation conditions in the line-emission nebulae and needs to be derived from near-infrared spectroscopy.

References

Acosta Pulido, J. A., Ballesteros, E., Barreto, M., et al. 2003, The Newsletter of the Isaac Newton Group of Telescopes, 7, 15
Anglada, G., Estalella, R., Rodriguez, L. F., et al. 1991, ApJ, 376, 615
Anglada, G., Rodriguez, L. F., & Torrelles, J. M. 1996, ApJ, 473, L123
Carrasco-González, C., Anglada, G., Rodríguez, L. F., et al. 2008, ApJ, 676, 1073
Davis, C. J., Whelan, E., Ray, T. P., & Chrysostomou, A. 2003, A&A, 397, 693
Fang, M., van Boekel, R., Wang, M., et al. 2009, A&A, 504, 461
Girart, J. M., Estalella, R., Anglada, G., et al. 1997, ApJ, 489, 734
Girart, J. M., Rao, R., & Estalella, R. 2009, ApJ, 694, 56
Goldsmith, P. F., Snell, R. L., Hemeon-Heyer, M., & Langer, W. D. 1984, ApJ, 286, 599
Hayashi, M., & Pyo, T.-S. 2009, ApJ, 694, 582
Hodapp, K.-W. 1994, ApJS, 94, 615
Lee, C.-F., Mundy, L. G., Stone, J. M., & Ostriker, E. C. 2002, ApJ, 576, 294
López, R., Estalella, R., Gómez, G., & Riera, A. 2006, A&A, 454, 233
López, R., Estalella, R., Gómez, G., Riera, A., & Carrasco-González, C. 2009, A&A, 498, 761
Manchado, A., Barreto, M., Acosta-Pulido, J., et al. 2004, Proc. SPIE, 5492, 1094
Nisini, B., Caratti o Garatti, A., Giannini, T., & Lorenzetti, D. 2002, A&A, 393, 1035
Nisini, B., Bacciotti, F., Giannini, T., et al. 2005, A&A, 441, 159
Palacios, J., & Eiroa, C. 1999, A&A, 346, 233
Reach, W.T., Megeath, S.T., Cohen, M. et al. 2005, PASP, 117, 978
Reipurth, B. 1994, A general catalogue of Herbig-Haro objects, Electronic version 1994-1
Reipurth, B., Yu, K. C., Heathcote, S., et al. 2000, AJ, 120, 1449
Vrba, F. J., Luginbuhl, C. B., Strom, S. E., et al. 1986, AJ, 92, 633